

# Dirac points and Weyl phase in a honeycomb altermagnet

Meng-Han Zhang , Xuan Guo , and Dao-Xin Yao\*

Guangdong Provincial Key Laboratory of Magnetoelectric Physics and Devices, State Key Laboratory of Optoelectronic Materials and Technologies, Center for Neutron Science and Technology, School of Physics, Sun Yat-Sen University, Guangzhou, 510275, China

\*yaodaox@mail.sysu.edu.cn

## ABSTRACT

We present a graphene derivative displaying novel topological phenomena without the spin-orbit coupling (SOC) in a collinear altermagnet. Band degeneracies in spin-split honeycomb antiferromagnets produce unique distribution patterns of Berry curvature and give rise to topological boundary states with unconventional spin textures. The asymmetric Berry curvature due to spin splitting can be created by lifting the degeneracies, which concentrate intensely at Weyl points contributing to carrier dynamics with a large valley Hall effect. The altermagnetism breaks the intrinsic time-reversal symmetry, guaranteeing the formation of pairs of Weyl points associated with the internal spin structure chiralities. We investigate the evolution of Dirac and Weyl crossings, in which topological phase transitions are characterized by the high Chern numbers preserving the non-intersecting flows of Wannier centers over occupied bands. Our results yield unique degeneracy-protected states by leveraging the symmetry constraints, where corresponding experiments are illustrated to demonstrate the potential of advancing valleytronic devices via unconventional topological responses.

Band degeneracies can produce highly localized Berry curvatures in spin-split structures preserving symmetry-constrained zero net magnetization, which manifest notable transport phenomena due to the anomalous valley Hall effect<sup>1-4</sup>. Since unconventional spin textures break time-reversal symmetry, chiral nodal lines and Weyl nodes emerge in two-dimensional collinear altermagnets even without spin-orbit coupling (SOC)<sup>5,6</sup>. We explore a graphene derivative in wallpaper group  $p6mm$  with the mirror and six-fold rotation symmetry, modifying the distribution of Berry curvature via staggered spin configuration and coupling strength<sup>7-9</sup>. The formation of gapless chiral edge states and dissipationless spin currents is imposed by lifting the band degeneracy at a general position, where intrinsic anomalous Hall effects (AHE) induce quantized transport responses<sup>10</sup>.

We investigate the spin current generation triggered by momentum-dependent spin splitting rather than the relativistic SOC, realizing emergent topological phases via four-sublattice bond dimerization<sup>11-13</sup>. The collinear antiferromagnetic orderings in a hexagonal cluster can be categorized into  $d_{x^2-y^2}$  or  $i$ -wave altermagnet owing to parity-time ( $PT$ ) symmetry in the honeycomb monolayer<sup>14</sup>, which differs from the majority of  $d_{xy}$  and  $g$ -wave symmetries<sup>15-17</sup>. When SOC is neglected, we demonstrate tilted Dirac cones and pairwise Weyl nodes by focusing on the cluster geometry and altermagnetic configuration<sup>18-20</sup>. The perturbation facilitates the unfolding of Dirac cones along high-symmetry paths in the first Brillouin zone (BZ), inducing a flow of Dirac cones to merge and annihilate each other via the dimerization of hopping terms<sup>21,22</sup>. We calculate the Hall conductivity grounded in a tight-binding model formed by hexagonal clusters, where the behaviors of valley-polarized currents are imposed by the gapped nodes in altermagnetic structure<sup>23</sup>. When integrated

with proximity-induced superconductivity, the pairing symmetries and finite-momentum pairing in altermagnets offer a fertile ground for researching novel topological phases and superconducting behaviors<sup>24,25</sup>.

The spectrum of nanoribbons supports localized edge states that span the whole zigzag terminations with pronounced van Hove singularities (vHSs), while the armchair configurations exhibit more uniform band structures rather than sharp spikes in the density of states (DOS)<sup>26</sup>. We align two ribbons with complementary bond patterns to ensure effective overlap and conjugation of the edge states, promoting efficient state mobility dynamically via geometric or bond modulation<sup>27-29</sup>. The strong-weak bonds alter the quantum interference between electron wavefunctions, contributing to the localization of edge states for quenching kinetic energy. Our research elucidates the intricate interplay between altermagnetism and topological phases, providing a promising platform for highly efficient spintronics devices that are not confined to heavy-element materials<sup>30,31</sup>.

## Altermagnetic wallpaper groups

Exploring beyond monolayer graphene, two-dimensional (2D) honeycomb altermagnets have captured growing research interest, particularly for their unique low-energy physics governed by Dirac-like electronic dispersions<sup>11</sup>. We construct a spin-wallpaper group  $p6mm$  in the absence of supercell, respectively flipping the spin on mirror and rotational symmetries related with two opposite-spin mapped to each other<sup>32,33</sup>. Preserving macroscopic net zero magnetization, the antiparallel orientation of magnetic moments interacts differently with the up and down spin states, which incorporate six-fold rotation from screw axis and the time-reversal symmetry ( $-i\sigma_y K$ )<sup>34</sup>. Additionally, we expand the unit cell to four sublattices via

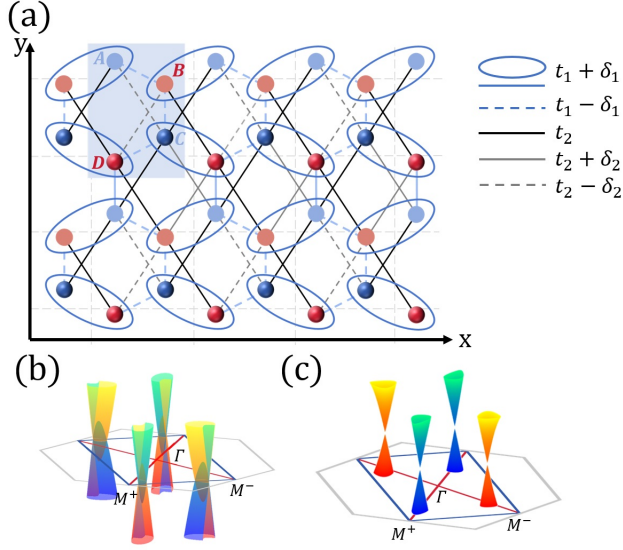


**Figure 1.** (a) Schematic of the honeycomb-lattice model for altermagnetism in group  $p6m$ . The model has four sublattices at each lattice point with red and blue dots denoting anti-aligned moments. The blue dashed lines represent the nearest-neighbor (NN) hopping strengths  $t_1 - \delta_1$ , and ellipses accompanied with blue lines are hopping terms with negative signs  $t_1 + \delta_1$ . The crystalline environment generates anisotropic second-nearest-neighbor hopping (black solid and dashed lines)  $t_2$  and  $\delta_2$ . (b) Dirac crossings with spin-up and spin-down bands develop on the BZ edges. (c) Weyl points between bands of the same spin are shown in red and blue, respectively. The massless crossings along the high-symmetry directions  $\Gamma - M$  annihilate each other into quadratic crossings with bands of opposite mirror  $M_x$  eigenvalues  $\pm 1$ .

spin flip and mirror reflection of glide plane, remaining the time-reversal invariant points  $\Gamma$  and  $M$  in the reduced half BZ. The symmetry of 2-fold spin rotation maintains the integrity of energy bands allowing for a variety of intriguing topological phenomena and anisotropic transport properties<sup>36–40</sup>.

We delve into the spectral properties of collinear anti-ferromagnet by manipulating the position and properties of the Dirac cones through hopping strengths, which eventually merge at high symmetry points to transform the semimetallic state into an insulating state<sup>39,40</sup>. Considering four distinct sublattices related by six-fold rotation as shown in fig. 1, the cell-periodic Hamiltonian is given by

$$\begin{aligned}
 H_0(\mathbf{k}) = & \tau_0 \otimes 2t_1 [\cos(k_1) \cos(k_2) \tau_x + \cos(k_1) \sin(k_2) \tau_y] \\
 & - \tau_z \otimes 2\delta_1 [\sin(k_1) \sin(k_2) \tau_x - \sin(k_1) \cos(k_2) \tau_y] \\
 & + \tau_x \otimes t_1 [\cos(2k_2) \tau_x - \sin(2k_2) \tau_y] \\
 & - \tau_y \otimes \delta_1 [\sin(2k_2) \tau_x + \cos(2k_2) \tau_y],
 \end{aligned}$$

(1)

where  $\mathbf{k}_1 = \frac{\sqrt{3}}{2} \mathbf{k}_x$ ,  $\mathbf{k}_2 = \frac{1}{2} \mathbf{k}_y$ , and  $\tau_i$  are Pauli matrices acting on the lattice degree of freedom. We reduce the model to a pristine graphene structure with a bulk energy gap closing along the boundary of BZ when  $\delta_1 = 0$ , exhibiting topologically protected linear crossing around the high-symmetry points  $(\pm \frac{\pi}{\sqrt{3}}, 0)$  shown in fig1. (b). The normal subgroup of group  $p6mm$  ensures that sublattice symmetries are maintained, where the interplay of mirror  $M_x$  and spin-rotational symmetries stabilizes the spin configurations contributing to the total magnetic moment compensation.

### Dimerized Model

The phase diagram with topological invariants outlines the transitions between trivial and topological semimetal phases, capturing the critical localization of robust edge states. We define the homeomorphism  $R^1 \cup \infty \rightarrow S^1$  to illustrate how dimerization generates tunable Dirac cones and induces phase transitions, where the parameter of vertical axis is  $\nu = \frac{\delta_1}{t_1}$  with a diameter of  $\sqrt{5}$ . As shown in Fig.2. (a), this mapping reveals a fundamental relationship between the dimerization strength and the emergence of massless Dirac fermions, which is protected by the combination of time-reversal symmetry and the bipartite nature of the lattice. The Dirac cones unfold along a high-symmetry path for a set of NN hoppings, eventually merging into a semi-Dirac point characterized at critical values  $\nu = 0, \pm \frac{\sqrt{5}}{5}, \pm \sqrt{5}, \infty$ . We highlight the highly anisotropic electronic properties via the convergence of Dirac cones, where direction-dependent behaviors can significantly influence electronic properties such as conductivity, transport responses, and the density of states near the Fermi level.

We exploit these modifications to preserve the propagation direction of robust edge conduction especially at interfaces, which originates in the two-dimensional Su-Schrieffer-Heeger (SSH) model for polymers. The emergence of Dirac cones  $(\pm \frac{1}{\sqrt{3}} \arccos \frac{\nu^2 + 3}{2\nu^2 - 2}, \frac{\pi}{3})$  at the BZ corners transforms the system back to the semi-metallic phase with the gap size  $2\sqrt{1 + 5\nu^2 - 2\nu\sqrt{5}}$ . Based on spinless electrons, the Hamiltonian can be decomposed via a  $2 \times 2$  block matrix  $h_0(\mathbf{k})$  defined as

$$t_1 \begin{bmatrix} (1 - \nu)e^{ia_1} + (1 + \nu)e^{-ia_2} & (1 + \nu)e^{2ik_2} \\ (1 - \nu)e^{-2ik_2} & (1 - \nu)e^{-ia_2} + (1 + \nu)e^{ia_1} \end{bmatrix}, \quad (2)$$

where  $\mathbf{a}_1 = \mathbf{k}_1 - \mathbf{k}_2$  and  $\mathbf{a}_2 = \mathbf{k}_1 + \mathbf{k}_2$ . Fixing  $k_2 = 0$ , the  $h_0(\mathbf{k}_1)$  is diagonalized into  $h_0^\chi(\mathbf{k}_1) = e^{-ik_1} + 1 + \chi \sqrt{\nu^2 (e^{-ik_1} - 1)^2 - \nu^2 + 1}$  through the chiral operator  $\chi$ . We derive the winding number as a topological invariant protected by chiral symmetry  $\chi = \tau_0 \otimes \tau_z$ .

$$w^\chi = \frac{1}{2\pi i} \int dk_1 \frac{d}{dk_1} \log h_0^\chi(\mathbf{k}_1), \quad (3)$$

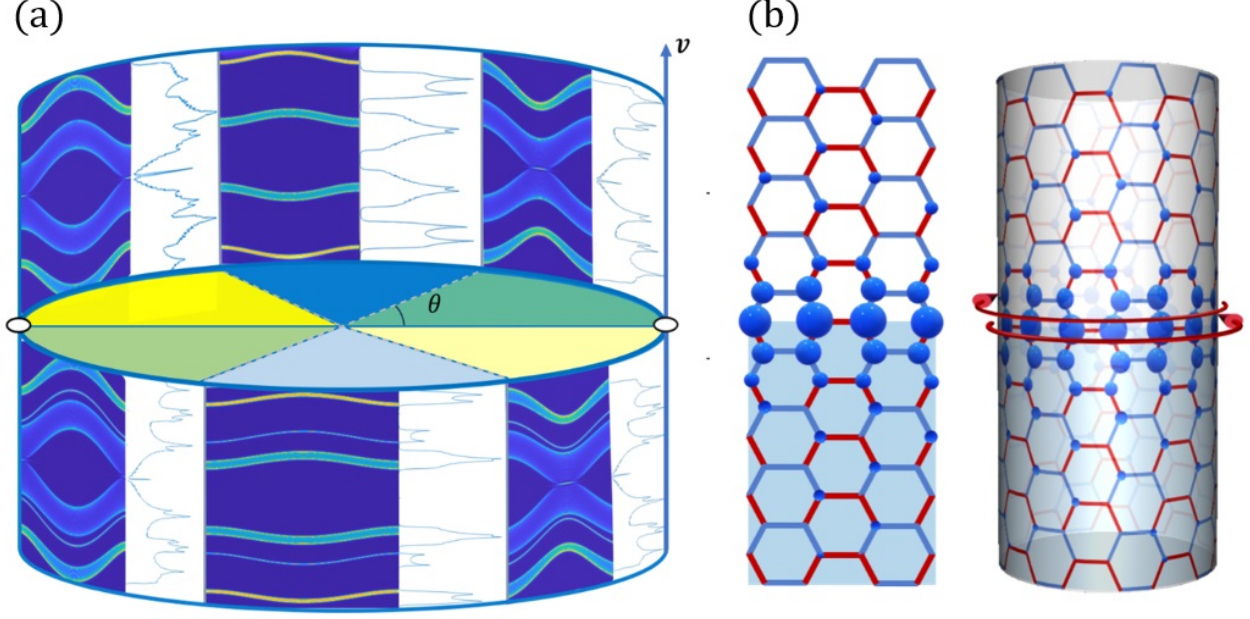


**Figure 2.** (a) Analytical demonstration of the phase diagram formed by  $\nu$  and  $\theta$ . The Dirac points merge together at the phase boundaries  $\theta = \pm \arctan \frac{\sqrt{5}}{2}$  and  $\pm(\pi - \arctan \frac{\sqrt{5}}{2})$ , where the spectral function of edge modes and DOS are depicted for each separated phase. (b) Two pairs of winding numbers with even and odd parity. The parameters of  $\nu$  are chosen at equal intervals from -1.2 to 1.2.

where the topological phase transition is quantized by the sign function  $sgn(\nu)$ , which characterizes a reversal in the chirality of edge mode. The spectrum of nanoribbons has zigzag edges along the  $k_1$  direction and armchair edges along the  $k_2$  direction, indicating the existence of propagating states along the transition interface. When  $\delta_1=0$ , the dispersion relation is simplified to four-band analytical structure  $E=\pm t_1 \sqrt{\Lambda(\mathbf{k}) \pm 2\sqrt{\lambda(\mathbf{k})}}$ .

$$\begin{aligned} \Lambda(\mathbf{k}) &= 1 + 4\cos^2(k_1) + \nu^2 [1 + 4\sin^2(k_1)], \\ \lambda(\mathbf{k}) &= [\cos^2(3k_2) + \nu^2 \sin^2(3k_2)] [4\cos^2(k_1) + 4\nu^2 \sin^2(k_1)] \\ &\quad + \nu^2. \end{aligned} \quad (4)$$

where two  $\pm$  signs distinguish the particle-hole symmetric branches corresponding to conduction and valence bands. We display the energy spectrum and density of states (DOS) for the edge modes in fig.2, while spatial distribution of the edge modes is depicted under the open boundary condition with 30 units in the perpendicular direction. Dimerization strengths and specific perturbations can drive the formation and unfolding of the Dirac cones, which are critical for developing next-generation transistors and sensors that leverage high mobility and unique electronic properties<sup>41</sup>.

### Anomalous Hall Effect

Extending the conventional anomalous Hall effect (AHE) that is predominantly observed in ferromagnetic structures, a

collinear altermagnetic honeycomb lattice with four sublattice arrangements  $A, B, C, D$  can inherently generate anomalous spin-polarized currents without necessitating a net magnetic moment. We consider the next-nearest-neighbor (NNN) hoppings to introduce anisotropy in the electronic structure by providing a mechanism for transfer that is sensitive to the momentum direction in the absence of SOC, which are  $S_1=2\delta_2 \sin(k_1) \cos(3k_2) \tau_y \otimes \tau_z$ ,  $S_2=-2\delta_2 \cos(k_1) \sin(3k_2) \tau_y \otimes \tau_0$  and  $S_3=4t_2 \cos(k_1) \cos(3k_2) \tau_x \otimes \tau_0$  respectively. The inclusion of NNN hoppings induces spin-split states that exhibit a strong momentum dependence, thereby altering distinctive spin currents with the adjustments in spin-valley interactions.

$$H_1(\mathbf{k}) = H_0(\mathbf{k}) + S_1 + S_2 + S_3. \quad (5)$$

We introduce the altermagnetism via anti-parallel magnetic moments ( $\mu=M_A - M_B=M_C - M_D$ ) from the hopping of itinerant electrons, which are sensitive to the staggered magnetization ( $\gamma=\tau_0 \otimes \tau_z$ ) inducing both ferroelectricity and magnetism. The localized spins interact with the itinerant electrons via the Kondo-like coupling  $\mu\gamma$  in two decoupled subspaces with well-defined spin, where  $\mu$  quantifies the interaction strength between the itinerant electrons and the collinear local moments with staggered magnetization. Thus, we construct an altermagnetic model from the  $\theta=\pi$  singularity of  $S^1$  in Fig. 2.

$$H(\mathbf{k}) = \sigma_0 \otimes H_1(\mathbf{k}) + \mu\sigma_z \otimes \gamma, \quad (6)$$

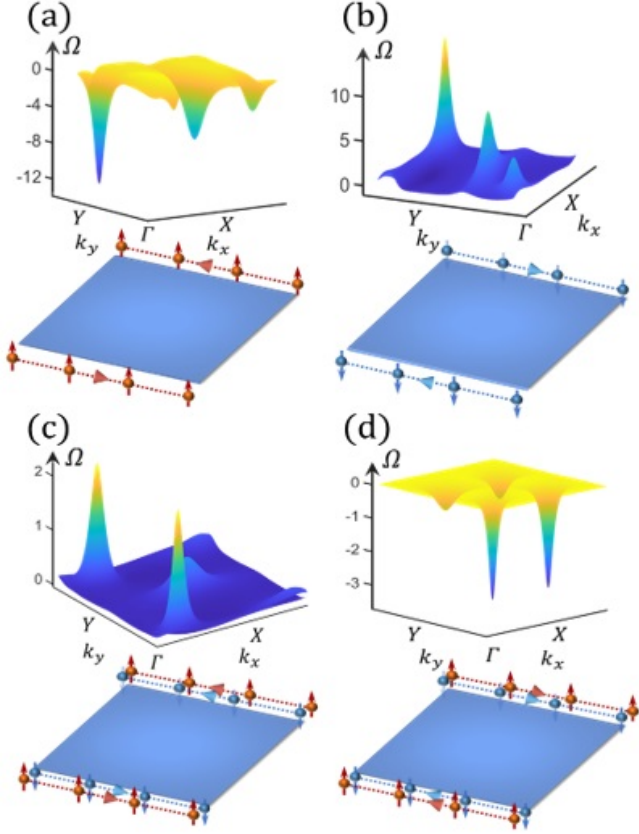


**Figure 3.** The distribution of Berry curvature in the limit of  $\nu \rightarrow \infty$ . (a) The directions of spin-up edge currents with  $C = 1$ . We use the parameters  $t_2=0.6$ ,  $\delta_2=1.2$ ,  $|\mu|=0.6$ , and set the coefficients of mass terms as  $m_1=1$ ,  $m_2=1.3$ . (b) The directions of spin-down edge currents with  $C=-1$ . We use  $\delta_2=-1.2$  setting the same other parameters as the former. (c) The spin-polarized current with  $C=2$ . We use the parameters  $t_2=0.6$ ,  $\delta_2=1.2$ ,  $|\mu|=4$  fixing the mass term  $m_2=0.3$ . (d) The spin-polarized current with  $C = -2$ . We use  $\delta_2 = -1.2$  with the same other parameters as the former.

where  $\sigma_i$  are Pauli matrices operating on the spin group. We calculate the energy spectrum for the  $\mu\gamma$  combined with staggered NNN hoppings as  $E^\chi = \chi\mu \pm 2\sqrt{4t_2^2 \cos^2(k_1) \cos^2(3k_2) + \delta_2^2 \sin^2(k_1 + 3\chi k_2)}$ . Lacking SOC the  $t_1$  term opens the altermagnetic nodal line to generate the spin-polarized Dirac cones as shown in fig. 2, where two spin-degenerate points can form a fourfold degeneracy with linear dispersion relations at the  $\delta_1=0$  critical point. We map the effective Hamiltonian into the subspace via the operator  $P = |\Psi^\alpha(\mathbf{k})\rangle \langle \Psi^\alpha(\mathbf{k})| \oplus |\Psi^\beta(\mathbf{k})\rangle \langle \Psi^\beta(\mathbf{k})|$ .

$$\begin{aligned} H_{q^\alpha} &= \epsilon_q^\alpha \sigma_0 + v_y^\alpha q_x^\alpha \sigma_y \pm v_x^\alpha q_y^\alpha \sigma_x, \\ H_{q^\beta} &= \epsilon_q^\beta \sigma_0 + v_y^\beta q_x^\beta \sigma_y \pm v_x^\beta q_y^\beta \sigma_x, \end{aligned} \quad (7)$$

where  $\epsilon_q^\alpha = \epsilon_q^\beta = 0$  represents half-filled Fermi energy. The

anisotropic velocities for spin-up subspace are  $v_x^\alpha$  and  $v_y^\alpha$ , where the counterparts for spin-down are represented by  $\beta$ . Owing to the horizontal mirror operation not swapping the sublattices, the bands of opposite spins hold tilted Dirac cones along the  $MX$  line with topologically protected 4-fold degeneracy. We derive the anisotropic velocities in the vicinity of pair-wise crossings  $(\pm \frac{\pi}{\sqrt{3}}, \pm \frac{\pi - \arccos \sqrt{\xi}}{3})$ .

$$\begin{aligned} v_y^\alpha &= v_y^\beta = \delta_2 \sqrt{3\xi}, \\ v_x^{\alpha\beta} &= \sqrt{|9\delta_2^2 - 9R^2 + \chi 18R^2 \cos^4 \frac{\sqrt{1-\xi}}{3}|}. \end{aligned} \quad (8)$$

where  $t_1$  reshapes the subspace algebraic structure via  $\xi = |\frac{R^2}{2\delta_2^2} - 1|$ ,  $R^2 = t_1^2 + \mu^2$ . We examine three distinct mass terms  $M_{\mathbf{k}} = m_1 \cos(2k_1) + m_2 \sin(2k_1) + m_3 \sin(2k_2)$  that maintain spin segregation by multiplying the general staggered hoppings with the lattice space operator  $\tau_z \otimes \tau_0$ , which avoids the mixing between spin-up and spin-down components to facilitate the formation of spin-polarized valleys. The altermagnetic potentials lift the spin-degeneracy at Dirac points to generate quadratic energy spectrum and total spin current, which takes the form  $j = \frac{\hbar}{2e} (j^\alpha + j^\beta)$  independently of SOC. Our results further emphasize the anisotropic NNN hoppings in generating quantized transverse Hall current, whose magnitude depends on the valley Hall effect in spin polarization<sup>42</sup>.

### Weyl Phase Diagram

We investigate the energy band splitting that facilitates the formation of linear crossings characterized by spin and lattice indices<sup>43</sup>, which remain isolated in momentum space as they evolve along high-symmetry directions<sup>44,45</sup>. Despite the presence of spin splitting, the net magnetic moment vanishes due to a combined symmetry that operates non-trivially on both spin and unit cell degrees of freedom<sup>46</sup>. The Weyl crossings between bands sharing the same spin but differing in sublattice indices undergo a topological transition<sup>19,20</sup>, generating massless fermionic excitations with well-defined chirality in the vicinity of these crossings<sup>47,48</sup>. The gapped Weyl crossings behave as valley-contrasting Berry curvature monopoles or antimonopoles determined by their chirality, effectively enabling nontrivial topology for the spin-splitting band structure along with various other unconventional transport phenomena<sup>49</sup>.

Within the Wilson loop framework, the evolution of Wannier function centers is governed by the  $U(2N)$  Berry connection  $A^{\alpha\beta}$ , while we project the  $H_0(\mathbf{k})$  into the Bloch occupied states via the position operator  $\sum_{\mathbf{k}} \sum_{\alpha,\beta=1}^{N_F} A^{\alpha\beta} |\Psi^\beta(\mathbf{k} + \delta_{\mathbf{k}})\rangle \langle \Psi^\alpha(\mathbf{k})|$ . The Wannier center flows are visualized in Fig. 4 using the non-Abelian Berry phase<sup>50,51</sup>, which arises from integrating the Berry curvature in fully decoupled spin subspaces. The Weyl phase diagram is formed by  $t_2$  and  $\delta_2$  in the configurational space with  $t_1$  fixed at 0 and  $\delta_1$  fixed at 1, where the topology of crossing is characterized by the Berry Phase  $\gamma_{\pm}^{\alpha(\beta)}$ .

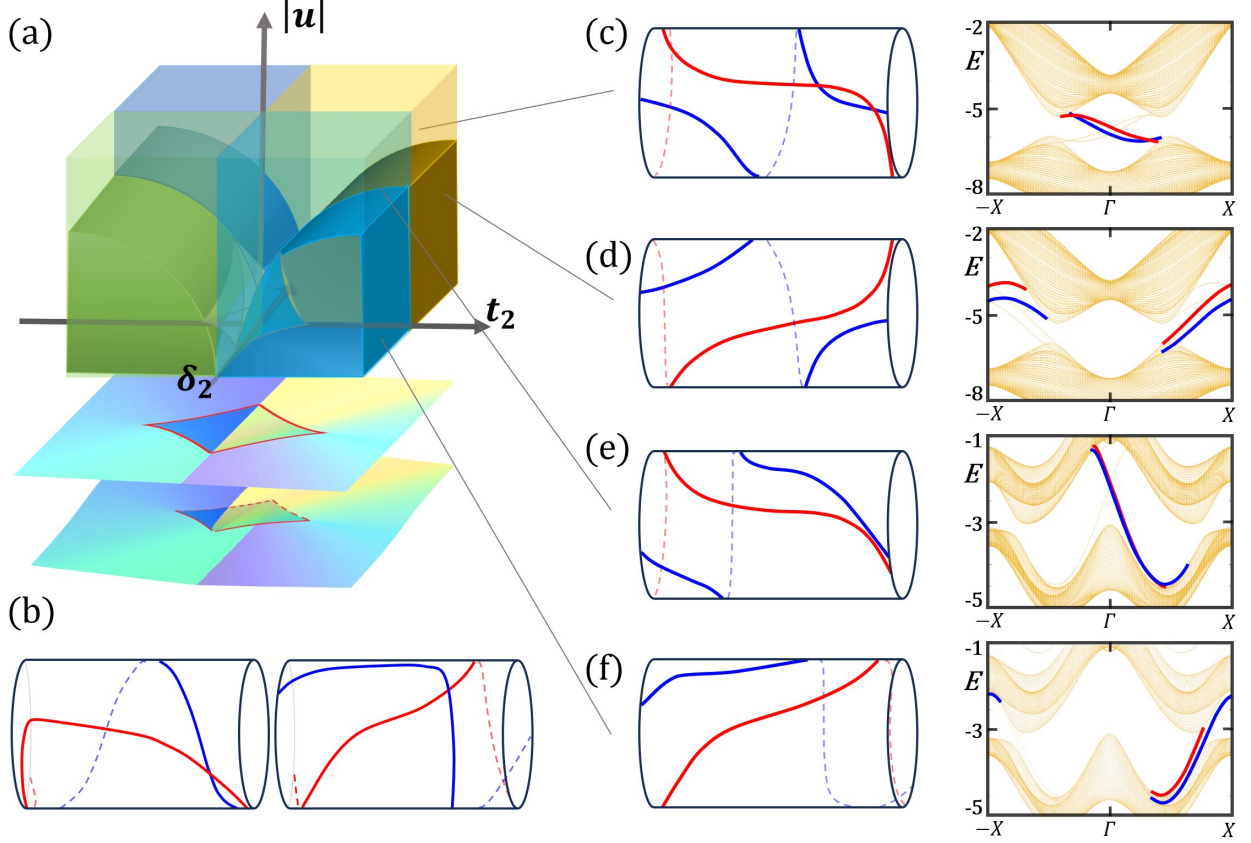


**Figure 4.** (a) The Weyl phase diagram demonstrates the formation of Weyl points, where the phase boundary is related to the singularity class when the map sends regular values to critical values. The number of Weyl points in the vertical axis is determined by the staggered potential  $\mu$ . (b) The flows of Wannier centers for  $|C|=1$  with equivalent parameter choices as fig. 3. (c)-(f) The curved surface separates the creation of weyl points from the gapped phase with  $|\mu|=0.6$ . The red line shows the chiral propagating states for spin-up, whereas the spin-down counterpart is in blue.

$$\begin{aligned}
 Y_{\pm}^{\alpha(\beta)} &= \pm \frac{1}{4\pi} \int_{BZ} \frac{\mathbf{d}_q^{\alpha(\beta)} \cdot [\partial_{q_x} \mathbf{d}_q^{\alpha(\beta)} \times \partial_{q_y} \mathbf{d}_q^{\alpha(\beta)}]}{|\mathbf{d}_q^{\alpha(\beta)}|^3}, \\
 &= \pm \frac{1}{4\pi} \int_{BZ} \frac{M_k v_x v_y}{2 \sqrt{v_x q_y^2 + v_y q_x^2 + M^2}} = \pm \frac{\text{sgn}(M_k)}{2},
 \end{aligned} \quad (9)$$

where  $\mathbf{d}_q^{\alpha(\beta)} = v_y^{\alpha(\beta)} \mathbf{q}_x + v_x^{\alpha(\beta)} \mathbf{q}_y + \frac{M_k}{2} \mathbf{q}_z$ . Fig. 4 displays representative phases modulated by adjusting the staggered magnetization as the control parameter, with distinct phase transitions exhibiting a clear dependence on the magnitude of parameter. We bridge a connection between the mappings of manifolds  $M^2 \rightarrow R^2$ , where  $R^2$  is two-dimensional Euclidean space. The emergence of pairwise Weyl points creates a cusp point from the map self-intersection, which are indicative of a topological phase transition<sup>52</sup>, accompanied by a divergence in the density of states near the Fermi level. The lifting of spin degeneracy enables unique chiral propagating states within the  $Z_2$  topological classification framework, producing quantized Hall conductance that exhibits unidirectional edge transport<sup>53</sup>.

We demonstrate that the zigzag edges of the altermagnetic ribbon are characterized by the antiparallel alignment of magnetic moments between adjacent sites, which induces a gap opening at the Weyl points. As illustrated in Fig. 4, the quantum Hall effect is theoretically calculated via the controlled fabrication of the valley degree of freedom in the altermagnetic band structure, which exhibits a pronounced spatial anisotropy confirmed by our Green's function analysis of edge states. The staggered magnetization profile localizes left-moving and right-moving modes on opposite edges, producing a dissipationless chiral edge current as demonstrated by our numerical solution of the Boltzmann transport equation<sup>54,55</sup>. Our findings suggest that high-energy photon injection can generate non-trivial topological states in our altermagnetic model, where the radiative recombination of spin-polarized carriers exhibits a net circular polarization<sup>56</sup>. Time-resolved Kerr rotation measurements reveal a helicity-dependent optical transition, which offers a direct experimental signature for probing the altermagnetic phase. Our results can also be realized in non-Hermitian systems through the modulation of gain and loss, facilitating resilient topological transport to

support promising applications for quantum computing even in the presence of controlled dissipation<sup>57,58</sup>.

## Possible experimental realizations

Allowing for the high *Néel* temperature, altermagnetism represents a cutting-edge frontier in the study of magnetic materials<sup>59–63</sup>, while the application of an out-of-plane electric field can modulate the magnetic interactions into more complex magnetic orderings<sup>64–66</sup>. The unique interplay of lattice symmetries suggests  $\text{MnP}(\text{S,Se})_3$  might be functionalized from a 2D antiferromagnet into a strong altermagnet<sup>67</sup>. The structural phase transition induced by chalcogen substitution modifies the exchange pathways, potentially creating the spin-split electronic bands characteristic of altermagnetic materials while preserving the compensated antiparallel spin arrangement. The particular  $C_2$  rotational symmetry of the Mn cation sublattice, combined with the ligand-field splitting induced by chalcogen substitution, creates the necessary conditions for alternating spin-polarized bands in both real and reciprocal space. Through precise strain engineering, this structural configuration may enable *Néel* temperatures surpassing room temperature, which would be significant for practical applications. The time-reversal symmetry breaking in monolayer FeSe is also not simply a manifestation of ferromagnetism but rather an indication of altermagnetism<sup>68,69</sup>, which offers strong evidence for this unconventional magnetic ordering phenomenon. Combined with the Kerr effect, the polarized photons interacting with the staggered magnetic moments can regulate topological responses in advanced optoelectronic devices<sup>70,71</sup>.

Ultracold atoms in optical lattices offer a highly controllable platform for studying altermagnetic topology<sup>72</sup>. The precise manipulation of atomic interactions and lattice geometries enables the emulation of exotic quantum phases, including those exhibiting altermagnetic order with non-trivial band topology. Based on broken time-reversal symmetry, our model can be realized in  $C_{6v}$ -symmetrical hexagonal lattices by breaking mirror symmetry, providing a versatile platform for the study of topological phenomena in elasticity. By tuning the lattice parameters, we can engineer our model into different topological regimes via artificial mechanical lattices, allowing for the observation of the robust transport for chiral edge modes. This tunability further allows for systematic exploration of topological phase transitions, including the formation of Dirac points and strain-induced band gap openings. Additionally, in ultracold atomic gases, the implementation of synthetic magnetic fields provides a controlled platform for engineering diverse topological phases and observing valley-dependent Hall effects<sup>3,4</sup>.

Topoelectrical circuits hold promise to manipulate the valley polarization through topological boundary resonances<sup>73,74</sup>. These circuit networks effectively mimic the valley-contrasting physics observed in 2D quantum materials, enabling selective excitation of valley-polarized states through appropriate impedance modulation. We consider a

honeycomb lattice structure with engineered parameters to achieve bond dimerization and onsite potentials. Weyl circuits exhibit tunable edge states governed by their intrinsic topology even without SOC, offering a promising platform for altermagnetic devices. The valley-contrasting transport properties emerge from the synthetic orbital magnetization patterns implemented, demonstrating that valley polarization can be achieved through purely orbital mechanisms without requiring spin-orbit coupling. The direction of propagation of the electromagnetic waves, representing the valley-polarized modes, depends on the handedness of the orbital angular momentum of the excitation source<sup>75–77</sup>. Furthermore, the edge state dispersion can be tuned by adjusting external circuit parameters, including capacitance and inductance values, while the valley index provides an additional degree of freedom for information encoding. Topoelectrical circuits exploit the inherent degeneracy to engineer robust states that are immune to backscattering and disorder, enabling the realization of valleytronic devices and the application of topological quantum computing<sup>78,79</sup>.

## Acknowledgements

We thank Zi-Jian Xiong, Zenan Liu for helpful discussions. This project is supported by NKRDPC-2022YFA1402802, NSFC-92165204, NSFC-12494590, Leading Talent Program of Guangdong Special Projects (201626003), Guangdong Provincial Key Laboratory of Magnetoelectric Physics and Devices (No. 2022B1212010008), Research Center for Magnetoelectric Physics of Guangdong Province(2024B0303390001), and Guangdong Provincial Quantum Science Strategic Initiative (GDZX2401010).

## References

1. Yuan, L.-D., Wang, Z., Luo, J.-W., Rashba, E. I. & Zunger, A. Giant momentum-dependent spin splitting in centrosymmetric low- $z$  antiferromagnets. *Phys. Rev. B* **102**, 014422 (2020).
2. Šmejkal, L., Sinova, J. & Jungwirth, T. Emerging research landscape of altermagnetism. *Phys. Rev. X* **12**, 040501 (2022).
3. Zhai, X. & Blanter, Y. M. Topological valley transport of gapped dirac magnons in bilayer ferromagnetic insulators. *Phys. Rev. B* **102**, 075407 (2020).
4. Xiao, D., Yao, W. & Niu, Q. Valley-contrasting physics in graphene: Magnetic moment and topological transport. *Phys. Rev. Lett.* **99**, 236809 (2007).
5. Zhu, Y.-P. *et al.* Observation of plaid-like spin splitting in a noncoplanar antiferromagnet. *Nature* **626**, 523 (2024).
6. Hayami, S., Yanagi, Y. & Kusunose, H. Momentum-dependent spin splitting by collinear antiferromagnetic ordering. *J. Phys. Soc. Jpn.* **88**, 123702 (2019).
7. Geim, A. K. Graphene: Status and prospects. *Science* **324**, 1530–1534 (2009).

8. Lin, Z. *et al.* Observation of giant spin splitting and d-wave spin texture in room temperature altermagnet  $\text{RuO}_2$ . *arXiv* 2402.04995 (2024).
9. Šmejkal, L., Sinova, J. & Jungwirth, T. Beyond conventional ferromagnetism and antiferromagnetism: A phase with nonrelativistic spin and crystal rotation symmetry. *Phys. Rev. X* **12**, 031042 (2022).
10. Fang, Y., Cano, J. & Ghorashi, S. A. A. Quantum geometry induced nonlinear transport in altermagnets. *Phys. Rev. Lett.* **133**, 106701 (2024).
11. Zeng, S. & Zhao, Y.-J. Description of two-dimensional altermagnetism: Categorization using spin group theory. *Phys. Rev. B* **110**, 2469–9969 (2024).
12. Liu, P., Li, J., Han, J., Wan, X. & Liu, Q. Spin-group symmetry in magnetic materials with negligible spin-orbit coupling. *Phys. Rev. X* **12**, 021016 (2022).
13. Chen, X. *et al.* Enumeration and representation theory of spin space groups. *Phys. Rev. X* **14**, 031038 (2024).
14. Chiu, C. K., Chan, Y. H. & Schnyder, A. P. Quantized berry phase and surface states under reflection symmetry or space-time inversion symmetry. *arXiv* 1810.04094 (2018).
15. Bhowal, S. & Spaldin, N. A. Ferroically ordered magnetic octupoles in d-wave altermagnets. *Phys. Rev. X* **14**, 011019 (2024).
16. Ding, J. *et al.* Large band-splitting in g-wave type altermagnet  $\text{CrSb}$ . *Phys. Rev. Lett.* **133** (2024).
17. Bühler, A. *et al.* Majorana modes and p-wave superfluids for fermionic atoms in optical lattices. *Nat. Commun.* **5**, 4504 (2014).
18. Li, C. *et al.* Topological weyl altermagnetism in  $\text{CrSb}$ . *arXiv* 2405.14777 (2024).
19. Liu, S. *et al.* Ferromagnetic weyl fermions in two-dimensional layered electride  $\text{gd}_2\text{C}$ . *Phys. Rev. Lett.* **125**, 187203 (2020).
20. Parshukov, K., Wiedmann, R. & Schnyder, A. P. Topological responses from gapped weyl points in 2d altermagnets. *arXiv* 2403.09520 (2024).
21. Zeng, M. *et al.* Observation of spin splitting in room-temperature metallic antiferromagnet  $\text{CrSb}$ . *Adv. Sci.* **11**, 2406529 (2024).
22. Sheoran, S. & Bhattacharya, S. Nonrelativistic spin splittings and altermagnetism in twisted bilayers of centrosymmetric antiferromagnets. *arXiv* 2310.19395 (2024).
23. Ezawa, M. Detecting the néel vector of altermagnets in heterostructures with a topological insulator and a crystalline valley-edge insulator. *Phys. Rev. B* **109**, 245306 (2024).
24. Zhang, S.-B., Hu, L.-H. & Neupert, T. Finite-momentum cooper pairing in proximitized altermagnets. *Nat. Commun.* **15**, 1801 (2024).
25. Zhu, D., Zhuang, Z.-Y., Wu, Z. & Yan, Z. Topological superconductivity in two-dimensional altermagnetic metals. *Phys. Rev. B* **108**, 184505 (2023).
26. Yu, Y., Suh, H.-G., Roig, M. & Agterberg, D. F. Altermagnetism from coincident van hove singularities: application to  $\kappa\text{-Cl}$ . *arXiv* 2402.05180 (2024).
27. Castro Neto, A. H., Guinea, F., Peres, N. M. R., Novoselov, K. S. & Geim, A. K. The electronic properties of graphene. *Rev. Mod. Phys.* **81**, 109–162, DOI: 10.1103/RevModPhys.81.109 (2009).
28. Jiang, Y. *et al.* Enumeration of spin-space groups: Toward a complete description of symmetries of magnetic orders. *Phys. Rev. X* **14**, 031039 (2024).
29. Brinkman, W. F., Elliott, R. J. & Peierls, R. E. Theory of spin-space groups. *Proc. Royal Soc. London. Ser. A. Math. Phys. Sci.* **294**, 343–358 (1966).
30. Yuan, L.-D., Wang, Z., Luo, J.-W. & Zunger, A. Prediction of low-z collinear and noncollinear antiferromagnetic compounds having momentum-dependent spin splitting even without spin-orbit coupling. *Phys. Rev. Mater.* **5**, 014409 (2021).
31. Han, L. *et al.* Electrical  $180^\circ$  switching of néel vector in spin-splitting antiferromagnet. *Sci. Adv.* **10**, eadn0479 (2024).
32. Šmejkal, L., Sinova, J. & Jungwirth, T. Beyond conventional ferromagnetism and antiferromagnetism: A phase with nonrelativistic spin and crystal rotation symmetry. *Phys. Rev. X* **12**, 031042 (2022).
33. Fu, L. & Kane, C. L. Topological insulators with inversion symmetry. *Phys. Rev. B* **76**, 045302 (2007).
34. Turek, I. Altermagnetism and magnetic groups with pseudoscalar electron spin. *Phys. Rev. B* **106**, 094432 (2022).
35. Teo, J. C. & Hughes, T. L. Topological defects in symmetry-protected topological phases. *Annu. Rev. Condens. Matter Phys.* **8**, 211–237 (2017).
36. Gao, Z.-F. *et al.* Ai-accelerated discovery of altermagnetic materials. *arXiv* 2311.04418 (2024).
37. Bernardini, F., Fiebig, M. & Cano, A. Ruddlesden-popper and perovskite phases as a material platform for altermagnetism. *arXiv* 2401.12910 (2024).
38. Miró, P., Audiffred, M. & Heine, T. An atlas of two-dimensional materials. *Chem. Soc. Rev.* **43**, 6537–6554 (2014).
39. Lee, Y.-L. Magnetic impurities in an altermagnetic metal. *arXiv* 2312.15733 (2023).
40. Ma, H. *et al.* Multifunctional antiferromagnetic materials with giant piezomagnetism and noncollinear spin current. *Nat. Commun.* **12**, 2846 (2021).

41. van Miert, G. & Ortix, C. Dislocation charges reveal two-dimensional topological crystalline invariants. *Phys. Rev. B* **97**, 201111 (2018).
42. Qi, X.-L., Wu, Y.-S. & Zhang, S.-C. Topological quantization of the spin hall effect in two-dimensional paramagnetic semiconductors. *Phys. Rev. B* **74**, 085308 (2006).
43. Chiu, C.-K., Teo, J. C. Y., Schnyder, A. P. & Ryu, S. Classification of topological quantum matter with symmetries. *Rev. Mod. Phys.* **88**, 035005 (2016).
44. Fedchenko, O. *et al.* Observation of time-reversal symmetry breaking in the band structure of altermagnetic  $\text{RuO}_2$ . *Sci. Adv.* **10**, eadj4883 (2024).
45. Antonenko, D. S., Fernandes, R. M. & Venderbos, J. W. F. Mirror chern bands and weyl nodal loops in altermagnets. *arXiv* 2402.10201 (2024).
46. Slager, R.-J., Mesaros, A., Juričić, V. & Zaanen, J. Interplay between electronic topology and crystal symmetry: Dislocation-line modes in topological band insulators. *Phys. Rev. B* **90**, 241403 (2014).
47. Nag, J. *et al.* Gdalsi: An antiferromagnetic topological weyl semimetal with non-relativistic spin splitting. *arXiv* 2312.11980 (2024).
48. Soto-Garrido, R., Muñoz, E. & Juričić, V. Dislocation defect as a bulk probe of monopole charge of multi-weyl semimetals. *Phys. Rev. Res.* **2**, 012043 (2020).
49. Chen, X., Wang, D., Li, L. & Sanyal, B. Giant spin-splitting and tunable spin-momentum locked transport in room temperature collinear antiferromagnetic semimetallic  $\text{CrO}$  monolayer. *Appl. Phys. Lett.* **123**, 022402 (2023).
50. Yamamoto, A. Berry phase in lattice qcd. *Phys. Rev. Lett.* **117**, 052001 (2016).
51. Xiao, D., Chang, M.-C. & Niu, Q. Berry phase effects on electronic properties. *Rev. Mod. Phys.* **82**, 1959–2007 (2010).
52. Re, L. D. Dirac points and topological phases in correlated altermagnets. *arXiv* 2408.14288 (2024).
53. Rhim, J.-W., Behrends, J. & Bardarson, J. H. Bulk-boundary correspondence from the intercellular zak phase. *Phys. Rev. B* **95**, 035421 (2017).
54. Šmejkal, L., González-Hernández, R., Jungwirth, T. & Sinova, J. Crystal time-reversal symmetry breaking and spontaneous hall effect in collinear antiferromagnets. *Sci. Adv.* **6**, eaaz8809 (2020).
55. Hoyer, R., Jaeschke-Ubiergo, R., Ahn, K.-H., Šmejkal, L. & Mook, A. Spontaneous crystal thermal hall effect in insulating altermagnets. *arXiv* 2405.05090 (2024).
56. Bao, C., Tang, P., Sun, D. & Zhou, S. Light-induced emergent phenomena in 2d materials and topological materials. *Nat. Rev. Phys.* **4**, 33–48 (2022).
57. Young, A. F. & Kim, P. Quantum interference and klein tunnelling in graphene heterojunctions. *Nat. Phys.* **5**, 222–226 (2009).
58. Wang, J., Chen, X., Zhu, B.-F. & Zhang, S.-C. Topological  $p$ - $n$  junction. *Phys. Rev. B* **85**, 235131 (2012).
59. Mazin, I. I., Koepernik, K., Johannes, M. D., González-Hernández, R. & Šmejkal, L. Prediction of unconventional magnetism in doped  $\text{feso}_2$ . *Proc. Natl. Acad. Sci.* **118**, e2108924118 (2021).
60. Guo, P.-J., Gu, Y., Gao, Z.-F. & Lu, Z.-Y. Altermagnetic ferroelectric  $\text{LiFe}_2\text{F}_6$  and spin-triplet excitonic insulator phase. *arXiv* 2312.13911 (2023).
61. Milivojević, M., Orozović, M., Picozzi, S., Gmitra, M. & Stavrić, S. Interplay of altermagnetism and weak ferromagnetism in two-dimensional  $\text{RuF}_4$ . *2D Mater.* **11**, 035025 (2024).
62. Mazin, I. I. Altermagnetism in  $\text{MnTe}$ : Origin, predicted manifestations, and routes to detwinning. *Phys. Rev. B* **107**, L100418 (2023).
63. Lee, S. *et al.* Broken kramers degeneracy in altermagnetic  $\text{MnTe}$ . *Phys. Rev. Lett.* **132**, 036702 (2024).
64. Hariki, A. *et al.* X-ray magnetic circular dichroism in altermagnetic  $\alpha$ - $\text{MnTe}$ . *Phys. Rev. Lett.* **132**, 176701 (2024).
65. Jang, B.-K. *et al.* Electric-field-induced spin disorder-to-order transition near a multiferroic triple phase point. *Nat. Phys.* **13**, 189–196 (2017).
66. RO, C. *et al.* Electric-field control of magnetic order above room temperature. *Nat. Mater.* **13**, 345–351 (2014).
67. Mazin, I., González-Hernández, R. & Šmejkal, L. Induced monolayer altermagnetism in  $\text{Mn}_2(\text{s,se})_3$  and  $\text{feso}_2$ . *arXiv* 2309.02355 (2023).
68. Wei, C.-C. *et al.*  $\text{La}_2\text{O}_3\text{Mn}_2\text{Se}_2$ : a correlated insulating layered d-wave altermagnet. *arXiv* 2410.14542 (2024).
69. Ezawa, M. Third-order and fifth-order nonlinear spin-current generation in  $g$ -wave and  $i$ -wave altermagnets and perfect spin-current diode based on  $f$ -wave magnets. *arXiv* 2411.16036 (2024).
70. Eschbach, M. *et al.* Realization of a vertical topological  $p$ - $n$  junction in epitaxial  $\text{Sb}_2\text{Te}_3/\text{Bi}_2\text{Te}_3$  heterostructures. *Nat. Commun.* **6**, 8816 (2015).
71. Ilan, R., de Juan, F. & Moore, J. E. Spin-based mach-zehnder interferometry in topological insulator  $p$ - $n$  junctions. *Phys. Rev. Lett.* **115**, 096802 (2015).
72. Das, P., Leeb, V., Knolle, J. & Knap, M. Realizing altermagnetism in fermi-hubbard models with ultracold atoms. *Phys. Rev. Lett.* **132**, 263402 (2024).
73. Huang, Y. & Chen, X. Quantum circuit complexity of one-dimensional topological phases. *Phys. Rev. B* **91**, 195143 (2015).

74. Ningyuan, J., Owens, C., Sommer, A., Schuster, D. & Simon, J. Time- and site-resolved dynamics in a topological circuit. *Phys. Rev. X* **5**, 021031 (2015).
75. Lee, C. H. *et al.* Topoelectrical circuits. *Commun. Phys.* **1**, 39 (2018).
76. Paler, A., Polian, I., Nemoto, K. & Devitt, S. J. Fault-tolerant, high-level quantum circuits: form, compilation and description. *Quantum Sci. Technol.* **2**, 025003 (2017).
77. Paler, A., Fowler, A. G. & Wille, R. Synthesis of arbitrary quantum circuits to topological assembly: Systematic, online and compact. *Sci. Reports* **7**, 10414 (2017).
78. Paler, A., Devitt, S. J., Nemoto, K. & Polian, I. Mapping of topological quantum circuits to physical hardware. *Sci. Reports* **4**, 4657 (2014).
79. Roushan, P. *et al.* Observation of topological transitions in interacting quantum circuits. *Nature* **515**, 241 (2014).